JOURNAL OF AIRCRAFT
Vol. 45, No. 4, July–August 2008

Effects of a Movable Tip Strake on Wake Vortex Structure

T. Lee*
McGill University, Montreal, Quebec H3A 2K6, Canada
and
V. Nikolic†
Minnesota State University, Monkato, Minnesota 56001

DOI: 10.2514/1.34620

The impact of a tip-mounted strake, set at different deflection angles relative to the main-wing chord plane on the near-field wake vortex structure, and the associated lift-induced drag were investigated experimentally at $Re = 191,000$. Force-balance aerodynamic forces were also obtained to supplement the wake vortex measurements. The results show that in addition to its substantial influence on the aerodynamic performance, the presence of the strake also led to an earlier completion of the rolling up of the tip vortex, compared with the baseline wing. The tip vortex had a reduced peak tangential velocity and core axial velocity but an increased core radius, compared with the baseline wing. These vortex core flow quantities increased with increasing strake angle δ. The core and total circulation increased above and remained below the baseline-wing value for $\delta > 5$ deg and $\delta < 5$ deg, respectively. The lift-induced drag, computed by using the Maskell induced-drag model, was found to increase nonlinearly with δ and became larger than the baseline wing for $\delta > 5$ deg.

Nomenclature

AR	=	aspect ratio
b	=	wing span, $2s$
C_D	=	drag coefficient
C_{Di}	=	lift-induced drag coefficient, $D_i/\frac{1}{2}\rho_\infty u_o^2 S$
C_L	=	lift coefficient, $L/\frac{1}{2}\rho_\infty u_o^2 S$
c	=	chord
D	=	drag force
D_i	=	lift-induced drag
e	=	span efficiency factor
L	=	lift force
M_∞	=	freestream Mach number
r_c	=	vortex core radius
r_o	=	vortex outer radius
Re	=	Reynolds number, $u_o c/\nu$
S	=	wing planform area
s	=	semispan
u, v, w	=	mean streamwise, vertical, and spanwise velocity
u_c	=	vortex core axial velocity
u_o	=	freestream velocity
v_θ	=	tangential velocity
x, y, z	=	streamwise, vertical, and spanwise direction
α	=	angle of attack
α_{ss}	=	static stall angle
Γ	=	vortex circulation
Γ_b	=	root circulation
Γ_c	=	core circulation
Γ_o	=	total circulation
δ	=	strake angle relative to wing chord plane
η	=	measurement grid size
ζ	=	streamwise vorticity
Λ	=	leading-edge sweep angle
ν	=	fluid kinematic viscosity
ρ_∞	=	freestream fluid density
ϕ	=	velocity potential
ψ	=	stream function

Received 17 September 2007; revision received 25 February 2008; accepted for publication 26 February 2008.

*Associate Professor, Department of Mechanical Engineering.
†Professor, Department of Mechanical Engineering. Associate Fellow AIAA.

I. Introduction

IT IS known that wing–fuselage strakes (also known as leading-edge extensions) usually decrease aerodynamic efficiency (i.e., lift-to-drag ratio); however, they improve high angle-of-attack performance by reducing separation on the main-wing panels and by generating vortex-induced lift. The addition of strakes also improves the maneuverability of future combat aircraft. An extensive review of wing-strake control is given by Nikolic [1]. Nikolic [1–3] further extended the wing-strake control concept to a rectangular wing of a NACA 4412 airfoil profile. The rectangular wing, with $c = 99$ mm, $b = 161$ mm, and AR $= 1.63$, was equipped with a movable tip strake (MTS) of eight different half-delta-wing configurations. All eight strakes had an incidental root chord nearly identical to that of the wing chord and a thickness of $2.5\%c$ and were attached to the $48.5\%c$ location of the wing chord. The effects of the MTS configuration and deflection angle (relative to the main-wing chord plane) on the lift and drag coefficients and the lift-to-drag ratio of the main wing were examined directly by using a wind-tunnel force balance at $Re = 225,000$. The MTS was found to consistently lead to an increased L/D ratio of the wing, mainly as a result of an increase in the wing aspect ratio and the vortex lift (induced by the strong vortices created along the swept leading edges). The leading-edge vortices (LEVs) progressed downstream, subjecting the wing suction surface to high rotational velocity and thus further increasing its lift and the accompanied lift-induced drag. It was hypothesized that the induced drag was, however, favorably affected by the increased wing aspect ratio. The measurements further concluded that the straight half-delta strake (with $\Lambda = 67.5$ deg) set at a zero deflection angle, was, however, found to be the most potent generator of additional vortex lift among the configurations tested for $\alpha \geq 10$ deg. When deflected relative to the main wing in the negative or positive sense, the strake led to added aerodynamic effects of the wing at higher or lower angles of attack, respectively. It is of interest to note that the strake deflection angle (set at an optimal for any α) further represents a new degree of freedom in controlling the aerodynamics of the wing's moveable-stake configuration. No detailed information of the velocity and vorticity flowfields of the

wake vortex, including the magnitude of the lift-induced drag, was reported, however.

The objective of the present experiment was to investigate the evolution of the vortex structure both along and in the near field behind a square-tipped rectangular NACA 0015 wing equipped with a straight half-delta strake with $\Lambda = 67.5$ deg at $Re = 191,000$ by using a miniature seven-hole pressure probe. This particular strake planform shape was chosen based on the findings of Nikolic [1]. Five strake settings, or deflection angles, were tested and the results were compared with those of the baseline, or clean, wing configuration. Special attention was given to the streamwise variation of the velocity and vorticity distributions and to the strength and size of the vortex with the strake setting. Lift-induced drag was also computed, based on the vorticity inferred from the measured crossflow velocity field, by using the Maskell induced-drag model. Wind-tunnel force-balance data were also obtained to supplement the vortex flow measurements. Physical mechanisms responsible for the observed vortex flow phenomena were also discussed.

II. Experimental Methods

The experiment was carried out in the $0.9 \times 1.2 \times 2.7$ m suction-type subsonic wind tunnel at McGill University with a freestream turbulence intensity of 0.05% at $u_o = 13$ m/s. A square-tipped rectangular wing of a NACA 0015 airfoil profile with $c = 20.3$ cm was used as the test model. The semispan of the half-wing model was $s = 50.8$ cm. The wing model was mounted horizontally at the center of the wind-tunnel test section. A circular end plate of 50-cm diameter with a sharp leading edge was fitted to one end, located 10 cm from the sidewall of the test section, of the wing model to isolate the free-end effects. The origin of the coordinate system was located at the leading edge of the wing. The semiwing model was also equipped with a moveable tip strake of a half-delta-wing shape with $\Lambda = 67.5$ deg. The strake had a chord of 20.3 cm, a semispan of 8.4 cm, an AR of 0.82, and a thickness of 5.5 mm (or 2.7%c). The strake gave rise to an 8.3% increase in the semiwing area. The aspect ratio of the half-wing and strake combination was 3.14. The leading edge was made sharp by applying a symmetric 45-deg bevel on both sides of the strake. The pivot axis was located at 45% of the wing chord from the leading edge. The gap between the wing tip and the strake was kept at 0.5 mm to minimize the flow leakage. Figure 1 shows the schematics and dimensions of the wing and the strake. The strake was set at five different settings ($\delta = +10$, $+5$, 0, -5, and -10 deg) relative to the wing chord plane. Positive and negative settings denote the strake leading edge up and down, respectively. The Reynolds number was fixed at 191,000.

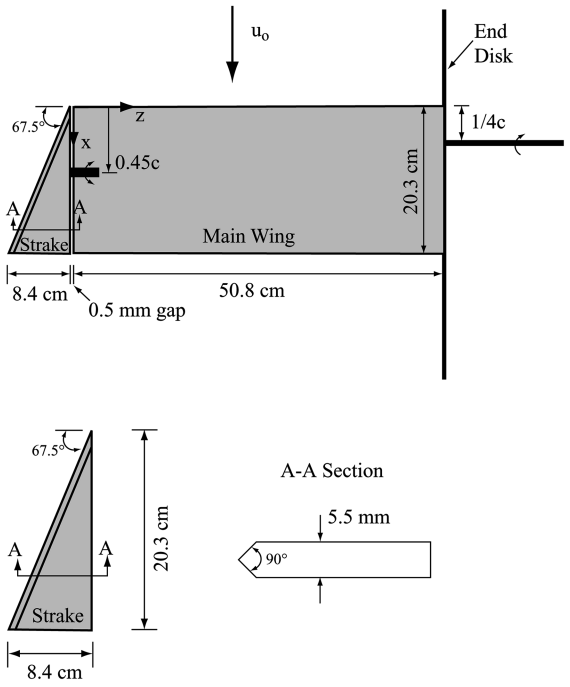

Fig. 1 Schematics of the MTS wing model.

The three components of the tip-vortex flow velocities were measured in planes perpendicular to the freestream velocity at nine x/c (0.5, 0.75, 0.9, 1.05, 1.5, 2, 2.5, 3, and 4) locations for $\alpha = 10$ deg, with and without the addition of the strake, by using a miniature seven-hole pressure probe with an outside diameter of 2.6 mm. For $x/c < 1$, the measurement planes were normal to the strake surface. The pressure probe was calibrated in situ before the installation of the model. Eight Honeywell model DC002NDR5 pressure transducers (seven for the probe and one for the tunnel reference total pressure) were used to maximize the data rate of the probe measurement system at each measurement location. The pressure signals were sampled at 500 Hz with a sampling time of 5 s and were recorded on a PC through a 16-bit A/D converter board. Probe traversing was achieved through a custom-built computer-controlled traversing system. Each data plane taken in the near field of the wing models had 2400 measuring grid points with an increment of $\Delta y = \Delta z = 3.2$ mm (or 1.6%c), except along the span of the wing, where $\Delta z = 6.4$ mm. A finer grid size of 1.2%c was also used to determine the core vortex flow characteristics. Figure 2a shows the adaptive grid method employed in the present experiment.

For lift and drag measurements, the finite wing model was mounted vertically on an external two-component force balance located below the wind tunnel. The wing model was mounted vertically above a $0.45 \times 60 \times 60$ cm aluminum end plate with sharp leading edges, fixed to the bottom wall of the test section, and an aerodynamic fairing was placed around the shaft to isolate it from the tunnel flow. The gap between the wing model and the end plate was kept at less than 1 mm to minimize leakage of flow through the gaps. The lift-induced drag coefficient C_{Di} was also computed based on the vorticity distributions inferred from the measured crossflow fields. The maximum uncertainty for the experimental data is as follows [4]:

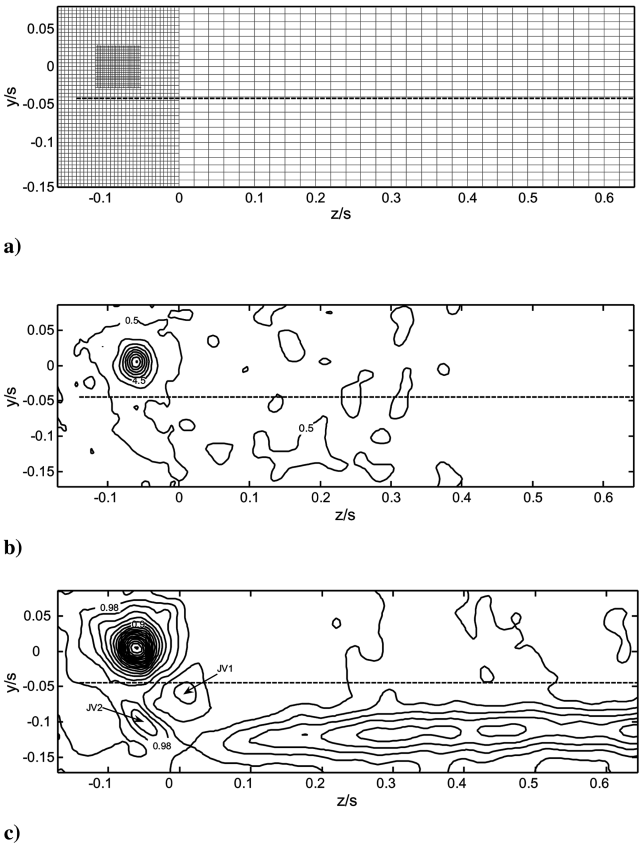

Fig. 2 Plots of a) adaptive grid and the wake measurement region, and b–c) normalized isovorticity and axial velocity contours of the MTS wing at $x/c = 4$ with $\delta = 0$ deg and constant $\zeta c/u_o$ and u/u_o increments of 2 and 0.02, respectively; JV_1 and JV_2 denote junction vortices 1 and 2.

mean velocity 3.5%, vorticity component 8%, vortex radius 4%, and velocity fluctuation 3%. The uncertainty in C_L and C_D determinations were ± 0.01 and ± 0.009, respectively.

III. Results and Discussion

A. Effect of δ on Aerodynamic Force Coefficient

To better understand the impact of the tip-mounted strake on the wake vortex structure and the associated lift-induced drag, the variation of the aerodynamic force coefficients with the strake setting, or deflection angle, was reexamined first and is presented in Fig. 3. Figure 3a shows that the positive strake settings ($\delta = 0$, $+5$, $+10$ and $+15$ deg) always led to a gain in C_L over the baseline wing. The lift coefficient increased persistently with increasing positive δ in the low-α range; an 11, 19, 27, and 35% increase in C_L, for example, was observed at $\alpha = 5$ deg for $\delta = 0$, $+5$, $+10$ and $+15$ deg, respectively. However, depending on the magnitude of δ, the LEV may potentially undergo breakdown and lead to a loss in the vortex lift at high wing angles of attack. A close examination of Fig. 3a further reveals that, in comparison with the baseline wing, for the MTS wing with the strake set at $\delta = 0$ deg, there was an increase in the lift-curve slope for the low-α range (for $\alpha < 7$ deg), whereas the lift curve was shifted upward for the moderate-to-large α range (covering $\alpha \approx 7$ deg to α_{ss}). The stall angle remained unchanged and the poststall lift was of a higher value than the baseline wing. The observed increase in C_L in both the low and moderate-to-high α ranges for $\delta = 0$ deg could be attributed to the potential attached-flow lift, as a result of the presence of the strake, and also to the vortex lift induced by the existence of the leading-edge separation vortex, respectively. Note that with the assumption that flow attachment occurs on the upper surface of the slender delta wings, the total lift can be then calculated [5,6] as the sum of the attached-flow lift $C_{Lp}(=\kappa_p \sin\alpha\cos^2\alpha)$ and the vortex lift $C_{Lv}(=\kappa_v \sin^2\alpha\cos\alpha)$, where $\kappa_p = 4\tan^{0.8}\varepsilon$, which depends only on planform, $\kappa_v = \pi/\sin\Lambda$, and ε is the half-apex angle of the straight delta wing. It is of importance, however, to note that for the present MTS wing configuration, the observed increase in C_L could also be partially due to the increased AR as well as to the improvement in the suction pressure over the wing's upper surface near the tip region (a secondary effect induced by the strake leading-edge vortex). The MTS wing with $\delta = 0$ deg also led to an improved lift-to-drag ratio, compared with that of the baseline wing, throughout the whole α range tested (Fig. 3b). The gain in the L/D ratio was most pronounced for the moderate-to-high α range; a 15% increase in $(L/D)_{max}$ observed at $\alpha = 10$ deg was observed for $\delta = 0$ deg. Note also the persistently improved aerodynamic performance for $\alpha > \alpha_{ss}$, regardless of δ.

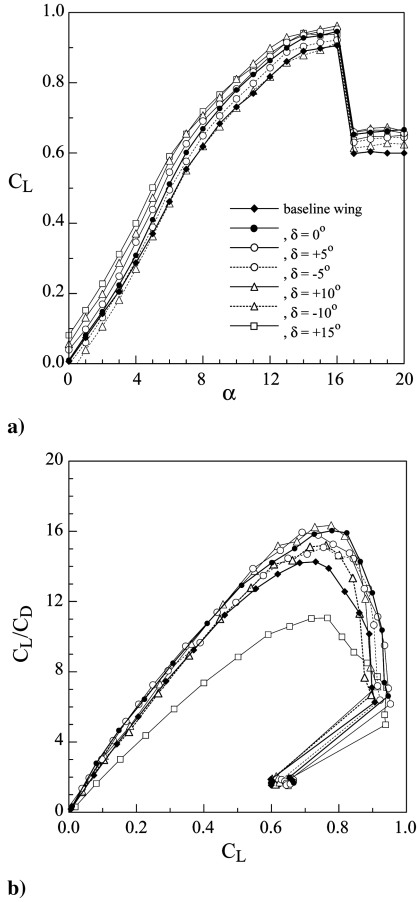

Fig. 3 Variation of C_L and C_L/C_D with δ and α.

For a positive strake setting larger than 0 deg, the lift curve was shifted vertically upward, mainly due to the vortex lift generated by the LEV. The presence of the strake also shifted the zero-lift angle of attack negative. The larger the positive strake setting, the higher the observed lift coefficient (before the occurrence of the LEV breakdown). Note that, in general, this vortex flow results in an increase in lift associated with the strake upper-surface pressures induced by the vortex and an increase in drag resulting from the loss of leading-edge suction. The higher the positive strake setting, the higher the wing drag thus observed at the same α. The C_D increased substantially, accompanied by the breakdown of the LEV. As expected, the aerodynamic performance of the MTS wing with $\delta = +15$ deg deteriorated overall because the increase in drag outweighs the gain in lift (Fig. 3b). Figure 3b also shows that the MTS wing with $\delta = 0$, $+5$, and $+10$ deg outperformed the baseline wing by a 13 to 15% margin from the lift-to-drag standpoint.

Figure 3a further reveals that at negative strake settings ($\delta = -5$ and -10 deg), the presence of the strake always gave rise to a reduced lift coefficient in the low-α range, compared with the baseline wing, and also a positive α_{zl}, as would be expected, because at those conditions, the strake generates lift force that is in the negative direction. For a $\delta = -5$ deg strake setting, the C_L was found to continuously increase above the baseline-wing value for $\alpha > 3$ deg; a trend similar to that of the $\delta = +5$ deg case, but of lower magnitude. For $\delta = -10$ deg, the lift coefficient remained virtually unchanged or reduced, compared with the baseline wing, for α ranging between 6 deg and α_{ss}, whereas the C_D was found to decrease below the baseline-wing value. Note that the reduction in C_D was largely responsible for the improved L/D ratio shown in Fig. 3b. The smaller the negative strake setting, the larger the lift-to-drag ratio. The aerodynamic gain in the L/D ratio produced by the negative strake setting was, however, of a lesser extent than with that of the corresponding positive strake setting. Finally, it is also of interest to note that the MTS wing always exhibited an unaffected stall angle, regardless of δ (Fig. 3a). This phenomenon could be due to the fact that the inboard lift (generated on the main-wing panel) overwhelmed the outboard lift increase or loss (caused by the presence of the strake). Meanwhile, it is known that the effect of δ on the C_D is twofold, by changing the wing form and friction drag and the lift-induced drag. The variation in the induced drag will be examined in Sec. III.C via the wake vortex flow measurements.

B. Effect of Strake on the Vortex Flow Structure

In this section, the tip-vortex structure was investigated, both along the tip (at $x/c = 0.5$, 0.75, and 0.9) and in the near wake behind the MTS wing (at $x/c = 1.05$, 1.5, 2, 2.5, 3, and 4) for $\delta = 0$ deg and $\alpha = 10$ deg. However, to reinforce the impact of the strake on the wake vortex structure, the formation and evolution of the tip vortex of the baseline wing at the same α was examined first and serves as a comparison.

Figure 4a shows the streamwise evolution of the normalized isovorticity contours of the baseline wing at $\alpha = 10$ deg. The presence of multiple secondary vortices around the tip at $x/c = 0.5$ (Fig. 4a) and its wrapping around the main vortex as it progressed down the chord can be clearly seen (Figs. 4b and 4c). The dashed line denotes the position of the wing's trailing edge. Immediately downstream of the trailing edge of the wing at $x/c = 1.05$ (Fig. 4d),

the vorticity from the shear layers leaving the trailing edge was rigorously carried into the vortex. The isovorticity contours, however, show asymmetric or developing patterns at this measuring station. Further downstream of the wing at $x/c = 1.5$ (Fig. 4e), the tangential velocity and vorticity distributions were attaining axisymmetry and the axial velocity deficit was reducing. Note that at $x/c = 1.5$, the tangential velocity was higher on the suction side by as much as 10% (i.e., with $v_{\theta\max} - |v_{\theta\min}| = 10\%u_o$). This discrepancy decreased rapidly with increasing x/c. At $x/c = 2$ (Fig. 4f), the inner region of the tip vortex was attaining axisymmetry. The degree of axisymmetry became more pronounced with the downstream distance. For $x/c \geq 2.5$ (Fig. 4g), the inner region of the vortex flow became nearly axisymmetric, with the magnitude of $v_{\theta\max}$ virtually equal to $|-v_{\theta\min}|$, whereas the flow outside the core region was still dominated by the remainder of the wing wake that wound into an ever-increasing spiral. The axisymmetric vortex flow behavior can be manifested from the normalized v_θ and ζ distributions across the vortex center (Figs. 5a and 5b).

For the MTS wing, the vorticity flowfield along the leading edge of the strake (Figs. 6a–6c) was found to be significantly different from that along the tip of the baseline wing (Figs. 4a–4c). In contrast to the presence of multiple secondary vortices and their entrainment into the main vortex along the tip of the baseline wing, an organized and strong strake leading-edge vortex was observed, accompanied by small secondary and tertiary vortices that were formed from separation of the upper surface under the primary or secondary vortex. The dashed line indicates the trailing edges of the wing and strake. The lightly shaded region in these figures and all subsequent figures denotes regions not reachable by the sensor probe, due to the geometric configuration of the wing-strake combination. The leading-edge vortex grew in strength and rotational velocity as it progressed downstream along the tip. Two junction vortices were also formed at the wing-strake junction (see, for example, Figs. 6b–6d). Note that the strake leading-edge vortex also energized the flow over the suction side of the main wing near the tip region and kept it attached to higher α (see Fig. 7a), except for the large separation region that occurred at the wing-strake junction. The present

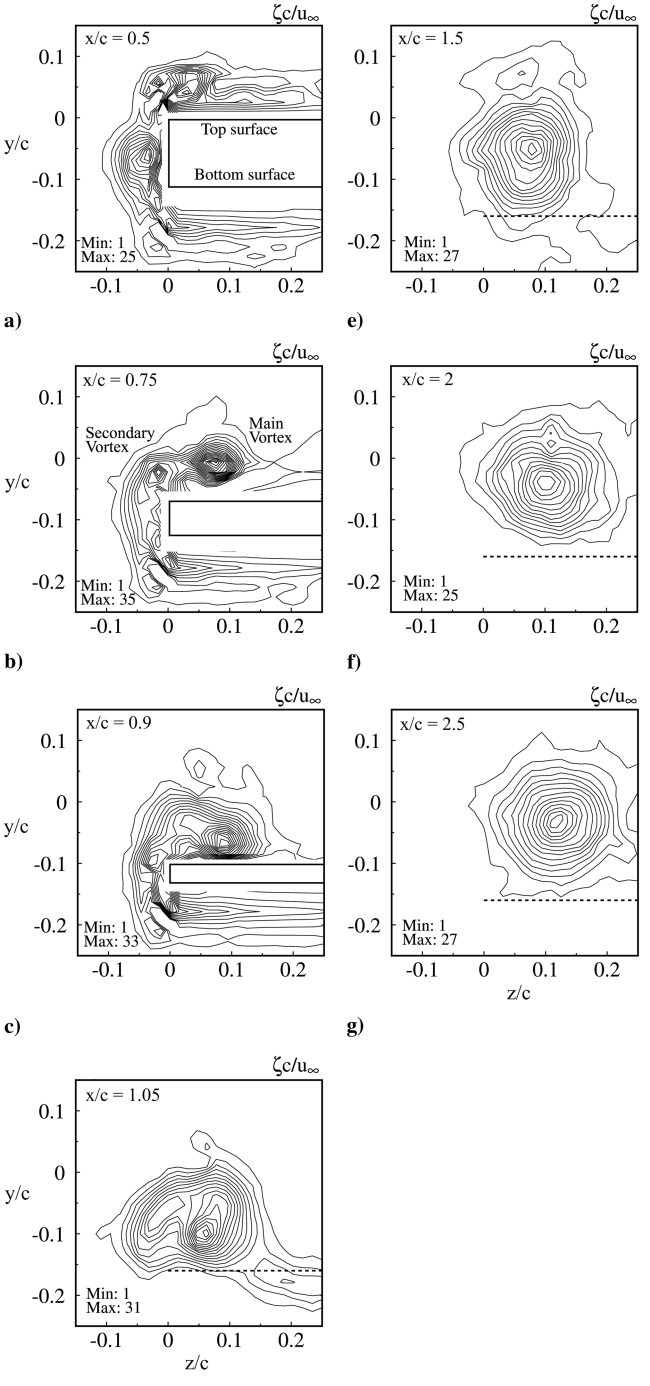

Fig. 4 Baseline-wing isovorticity contours at different x/c and a constant $\zeta c/u_o$ increment of 2.

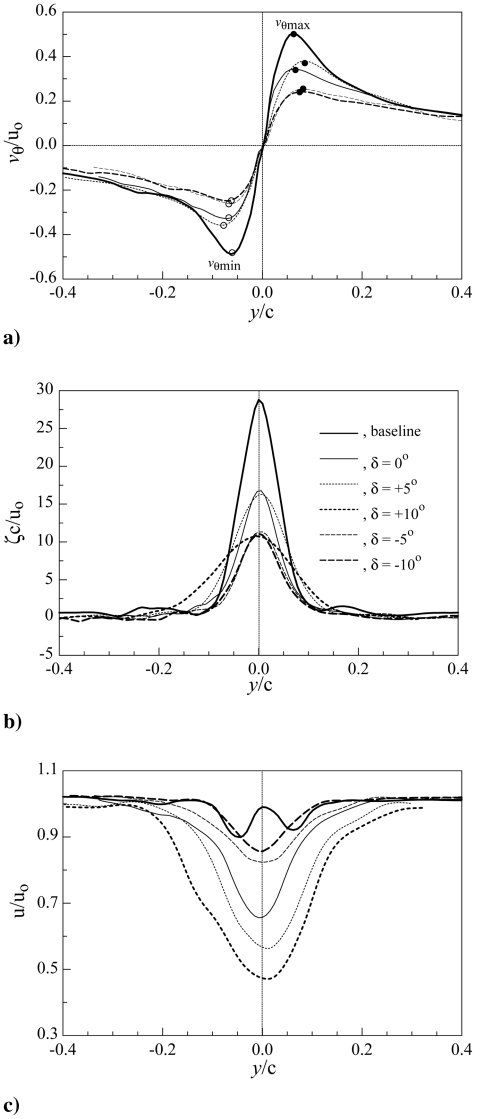

Fig. 5 Variation of normalized v_θ, u, and ζ distributions across the vortex center along the y axis with δ at $x/c = 4$ for $\alpha = 10$ deg. Solid circles denote $v_{\theta\max}$ and open circles denote $v_{\theta\min}$.

measurements further indicate that immediately downstream of the trailing edge of the MTS wing (i.e., at $x/c = 1.05$), the isovorticity contours exhibited a more organized vortical wake pattern (Fig. 6d), compared with the baseline wing at the same position (Fig. 4d), suggesting that the addition of the strake significantly modified the near-wake vortex roll-up and formation process. Note also that the inner region of the MTS vortex flow rapidly attained axisymmetry at $x/c = 1.5$ (Fig. 6e), compared with $x/c > 2$ of the baseline wing (Fig. 4g). No significant variation in overall behavior of the normalized isovorticity contours (Figs. 6e and 6f) was observed as the vortex progressed further downstream of the trailing edge of the MTS wing for $1.5 \leq x/c \leq 4$ tested. The relatively earlier completion of the roll-up process of the MTS tip vortex, compared with that of the baseline wing, can be further demonstrated from the iso-u/u_o contours displayed in Figs. 7b–7e. The normalized axial velocity contours reveal that even though the vorticity distribution behaved axisymmetrically at around $x/c = 1.5$ for the MTS wing (Fig. 6e), the axial velocity field did not complete its merger between the axial tip-vortex flow and the flow separated from the beveled leading edge of the strake until $x/c \approx 2.5$ (Fig. 7d). For $x/c \geq 2.5$, the axial velocity distribution behind the MTS wing always exhibited a bell-shaped wakelike velocity profile (see also Fig. 5c) with a core axial velocity u_c of $0.656u_o$, which is 33% smaller than the baseline-wing value. For the baseline wing, the iso-u/u_o contours were, however, found to form "islands" of wakelike velocity distributions (see Figs. 5c and 7f). The presence of islands in the wake distribution could indicate some remnant of individual vortices. Representative vw-vector plots at $x/c = 0.9$ and 4 (not shown here) further elucidate the presence of the strake LEV and the tip vortex in the near wake of the MTS wing.

The variation of the core vortex flow quantity of the MTS wing with x/c for $\delta = 0$ deg and $\alpha = 10$ deg was also obtained and is summarized in Fig. 8. The core radius and the total circulation of the MTS-generated tip vortex were persistently above the baseline-wing value and were also increased slightly with increasing x/c, due to the increased diffusion and vortex lift caused by the presence of the strake (Figs. 8a and 8b). An average value of r_c/c and Γ_o/cu_o of 0.074 and 0.281 and 0.065 and 0.25 were obtained for the MTS wing (for $x/c \geq 1.5$) and the baseline wing (for $x/c > 2$), respectively. Meanwhile, the peak tangential velocity (Fig. 8c) and vorticity (Fig. 8d) and the core circulation (Fig. 8e) and axial velocity (Fig. 8f) were persistently below those of the baseline wing. A minor decrease in $v_{\theta\text{peak}}$, ζ_{peak}, Γ_c, and u_c with x/c (for $x/c > 1.5$) was also noticed. At $x/c = 4$, the value of $v_{\theta\text{peak}}/u_o$, $\zeta_{\text{peak}}c/u_o$, Γ_c/cu_o, and u_c/u_o was found to be 0.312, 16.7, 0.145, and 0.61, which translates into a 36.5, 39, 27, and 38% reduction in $v_{\theta\text{peak}}$, ζ_{peak}, Γ_c, and u_c, compared with that of the baseline wing, respectively, at the same x/c. Note that the vortex was also found to be shifted further inboard and above the trailing edge of the MTS wing as it progressed downstream (Figs. 8g and 8h).

The present whole wake flow measurements (up to 80% of the span; Figs. 2b and 2c) also allow the determination of the root or bound circulation Γ_b from the spanwise circulation $\Gamma(z)$ distributed along the wing span (Fig. 9). The spanwise circulation distribution

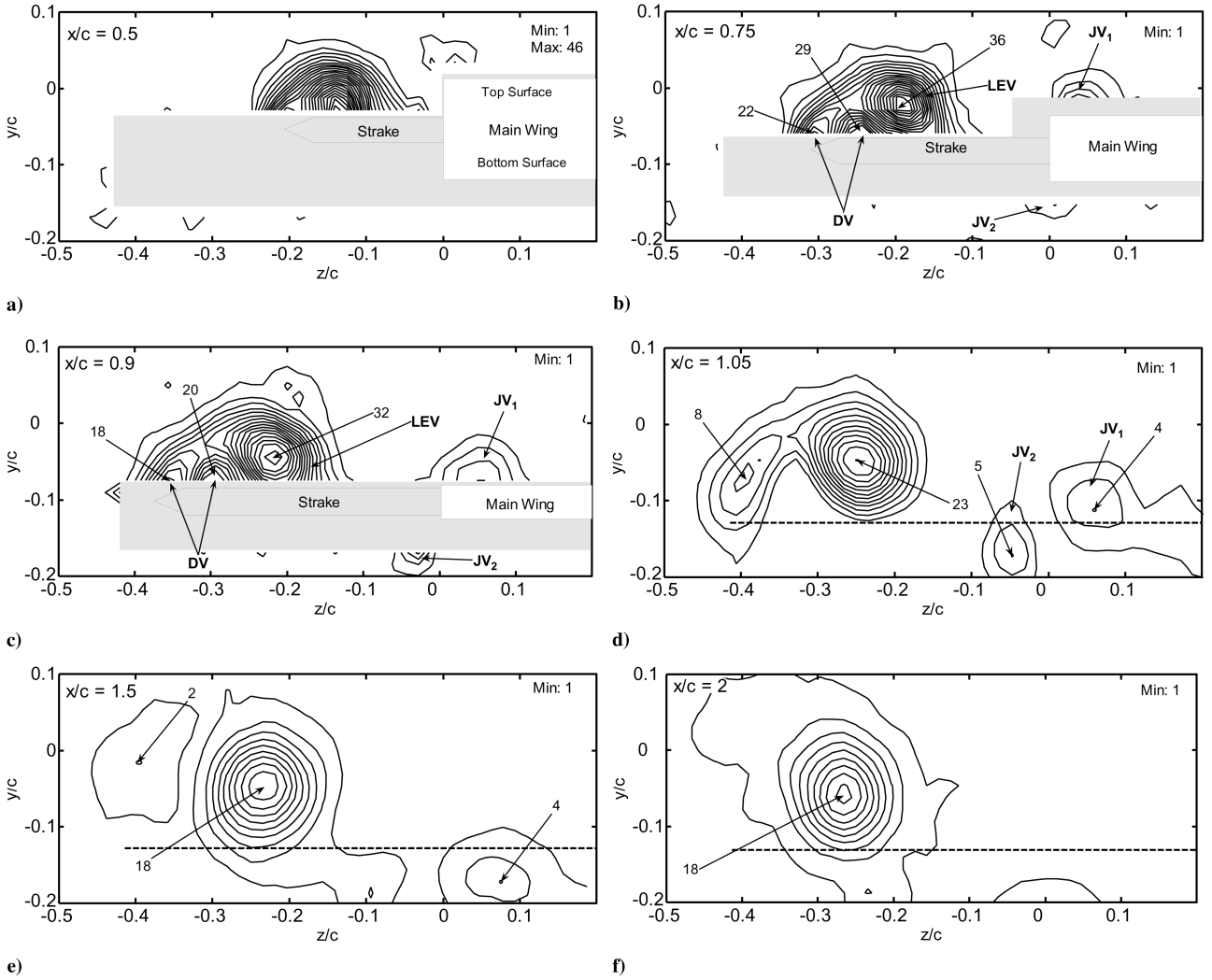

Fig. 6 Isovorticity contours at different x/c: a–i) MTS-wing with $\delta = 0$ deg, j) baseline-wing vw-vector plots of the MTS wing, k) $x/c = 0.9$, and l) $x/c = 4$; DV denotes the secondary and tertiary vortices, and JV_1 and JV_2 denote junction vortices 1 and 2.

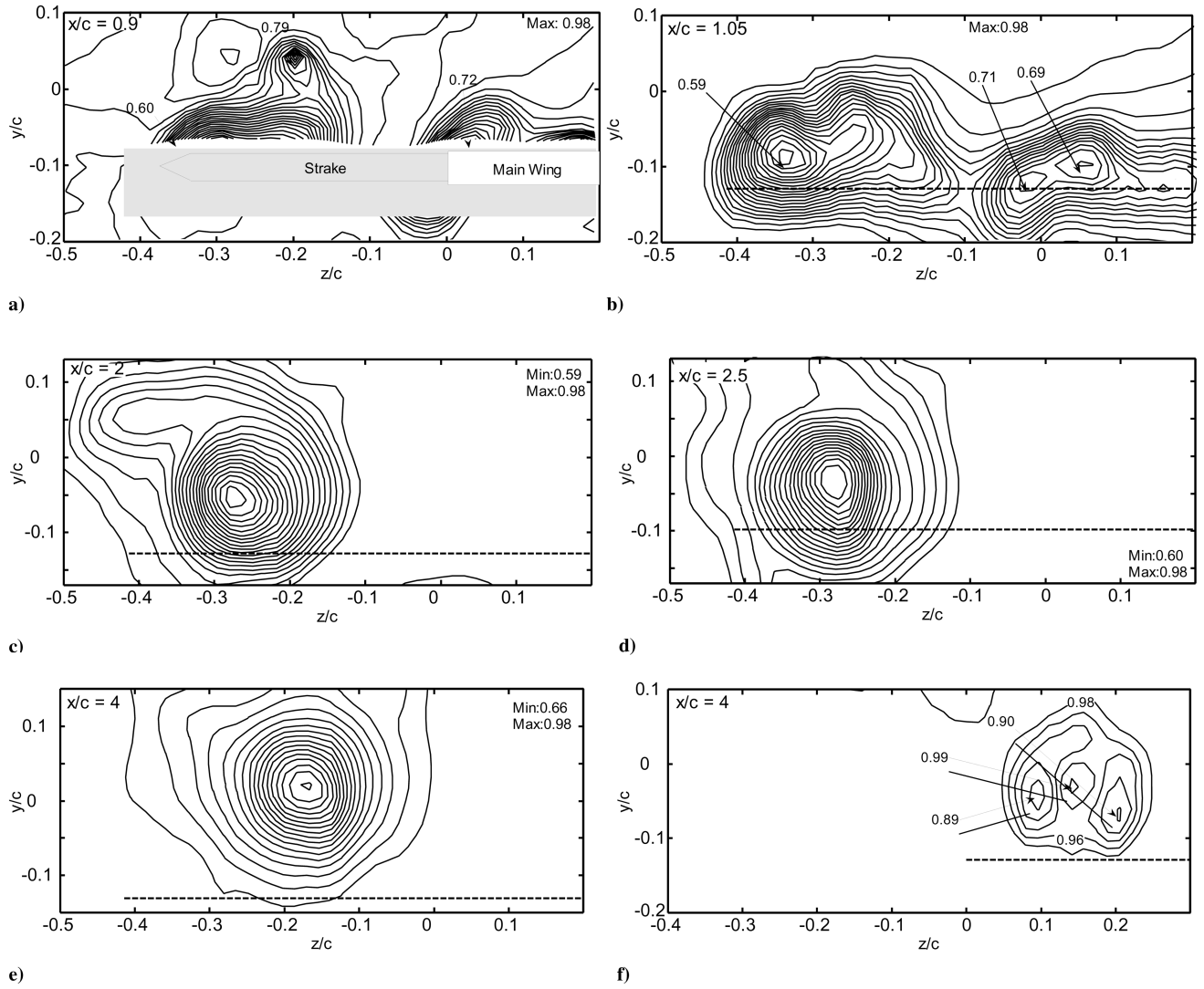

Fig. 7 Iso-u/u_o contours at different x/c: a–e) MTS wing with $\delta = 0$ deg and f) baseline wing.

was determined by computing the area integral of vorticity over the region of the scan outboard of z_i at each spanwise location z_i. Figure 9 also shows that there was a dip in $\Gamma(z)$ distribution near the tip for both the baseline wing and the MTS wing and that starting with the total bound circulation at the plane of symmetry ($z = s$), the vorticity was shed into the wake until the bound circulation was zero at the tip and fully converted into the wake circulation. More important, the value of Γ_b (at $z = s$) can be extrapolated from the spanwise $\Gamma(z)$ distribution. A normalized Γ_b/cu_o value of 0.365 and 0.385 for the baseline wing and the MTS wing with $\delta = 0$ deg was obtained. The Γ_b value also rendered an Γ_o/Γ_b ratio of 67 and 73% for the baseline wing and the MTS wing, respectively, which suggests that about 67 and 73% of the bound circulation was entrained into the vortex in the near wake behind these two wing models.

The effects of the strake setting ($\delta = -10, -5, +5$, and $+10$ deg) on the velocity and vorticity flowfields of the vortex at $x/c = 4$ for $\alpha = 10$ deg were also investigated and are elucidated in Figs. 10 and 11. The vortex size, strength, and trajectory were greatly influenced by the presence of the strake to various degrees, depending on the magnitude of δ. The vortex became more diffused and was displaced further outboard of the strake ($\delta = 5$ and 10 deg; Figs. 10a and 10b) with increasing positive strake settings, whereas the vorticity level and the axial wake deficit was reduced (Figs. 10d and 10e). A weakened vorticity level, accompanied by a reduced wake deficit, compared with the positive strake setting exhibited for the $\delta = -5$ deg strake setting (Figs. 10c and 10f). Detailed distributions of v_θ, ζ, and u across the vortex center are given in Figs. 5a–5c. Figure 11a shows that, as expected, the increase in C_L value with δ translates directly into a corresponding increase in the total circulation. The Γ_o value was increased somewhat linearly above the baseline-wing value, with δ for $\delta \geq +5$ deg. Figure 11a, in combination with Fig. 9, also rendered an Γ_o/Γ_b of 0.8, 0.78, 0.71, and 0.71 for $\delta = +10, +5, -5$, and -10 deg, respectively. The results also show that the Γ_b value determined from Fig. 9 was also found to be in good agreement with that estimated directly by using the $\Gamma_b/cu_o = \frac{1}{2}C_L$ relationship (see Table 1). The observed increase in Γ_o was also accompanied by a corresponding increase in Γ_c. The Γ_c value was, however, found to increase above the baseline-wing value for $\delta > 0$ deg (Fig. 11a): a trend similar to that of the lift-induced drag coefficient (to be discussed later in Sec. III.C). The vortex core radius was always above the baseline-wing value (Fig. 11b), regardless of δ, which further demonstrates that the presence of the strake consistently led to a wake vortex with an increased size and turbulent diffusion (i.e., a lowered peak vorticity; Fig. 11c), compared with the baseline wing. The increase in r_c and the reduction in ζ_{peak} was most pronounced with an increasing positive strake setting. For a negative strake setting, the ζ_{peak} was found to remain below the $\delta = 0$ deg value, but was decreased with an increasing negative strake setting. Meanwhile, the core radius exhibited a rise and fall with the decrease in the negative strake setting. A 34 and 82% increase and decrease in Γ_c and r_c, together with a 68% decrease in ζ_{peak}, was observed at $x/c = 4$ for a $\delta = +10$- deg strake setting. The value of $v_{\theta\text{peak}}$ and u_c of the MTS wing was always below the baseline-wing

value, regardless of δ (Figs. 11d and 11e). A considerable increase in $v_{\theta\text{peak}}$ (except for the $\delta = +10$-deg case) and a reduction in u_c with an increasing strake setting was also noticed. The present measurements also show that the tip vortex generated in the near-field behind the MTS wing was shifted further outboard with increasing δ, whereas it was generally displaced further below the trailing edge (Fig. 11f).

C. Lift-Induced Drag

The lift-induced drag D_i was computed by using the Maskell induced-drag model [7] based on the vorticity inferred from the measured velocity field. The crossflow velocity vectors within the measurement plane were decomposed into a stream function $\psi(y, z)$ and a crossflow velocity potential $\phi(y, z)$, with the imposed boundary conditions requiring both ψ and $\partial\phi/\partial n$ to be zero on the walls of the wind tunnel. The lift-induced drag was then obtained by [8–10]

$$D_i = \frac{1}{2}\rho_\infty \iint_{S_\zeta} \psi\zeta \,\mathrm{d}y\,\mathrm{d}z - \frac{1}{2}\rho_\infty \iint_{S_1} \phi\sigma \,\mathrm{d}y\,\mathrm{d}z - \frac{1}{2}\rho_\infty \iint (1 - M_\infty^2)(\Delta u)^2 \,\mathrm{d}y\,\mathrm{d}z \tag{1}$$

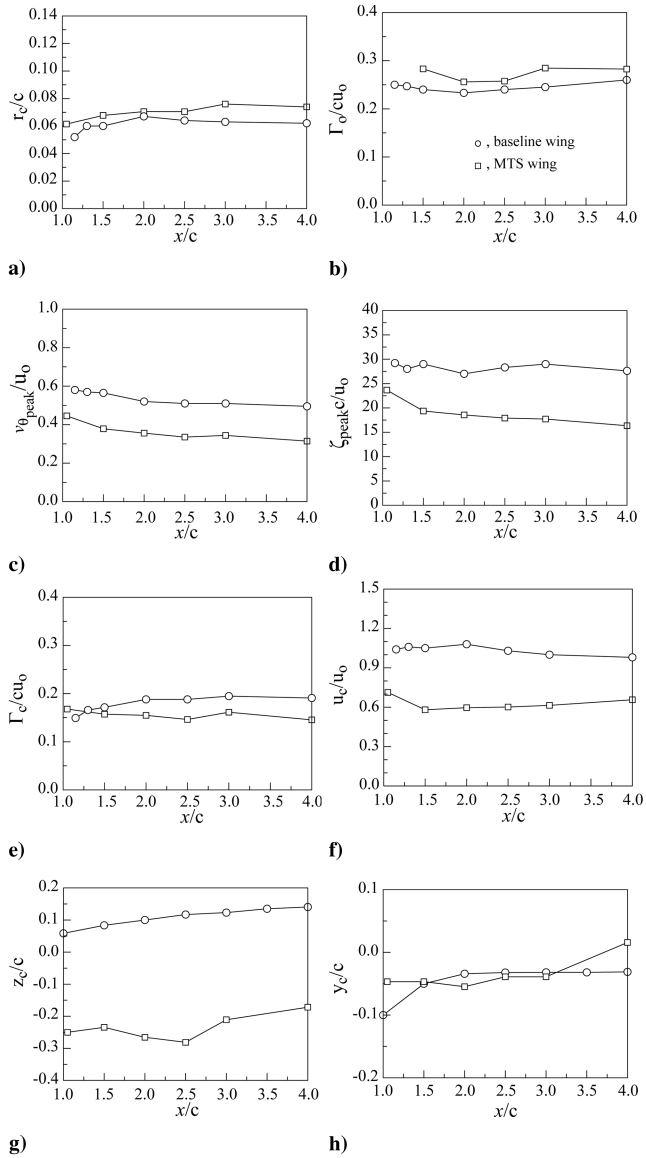

Fig. 8 Variation of critical vortex flow quantity with x/c for $\delta = 0$ deg and $\alpha = 10$ deg.

where $\zeta = \partial w/\partial y - \partial v/\partial z$ is the streamwise vorticity, the surface S_ζ is the region within S_1 where the vorticity is nonzero, and

$$\sigma = \partial v/\partial y + \partial w/\partial z = -\partial u/\partial x$$

is a source term that is small outside the viscous wake. Note that the third integral was introduced by Betz [11] and is usually assumed to be negligible. Two main routes exist in the determination of the stream function and velocity potential at each point in the scan. One scheme uses the velocity field by solving the following two equations at each measurement location: $v = \partial\psi/\partial z + \partial\phi/\partial y$ and $w = -\partial\psi/\partial y + \partial\phi/\partial z$. This may be expressed via a centered finite difference computational scheme, by letting

$$2\eta v_{j,i} = -\psi_{j,i-1} + \psi_{j,i+1} - \phi_{j-1,i} + \phi_{j+1,i}$$

and

$$2\eta w_{j,i} = \psi_{j-1,i} - \psi_{j+1,i} - \phi_{j,i-1} + \phi_{j,i+1}$$

for a given data set with uniform grid points (i.e., $\Delta y = \Delta z = \eta$). This method is slightly inconvenient, however, for two reasons: first, the known velocities are expressed as functions of both the unknown stream and velocity potential functions, and second, a total of $(2 \times n - 2 \times m - 2)$ equations with $(2 \times n - 2 \times m - 2)$ unknowns need to be solved simultaneously for a $(n \times m)$ size grid. Another more convenient scheme solves the Poisson equations $\partial^2\psi/\partial^2 y + \partial^2\psi/\partial^2 z = -\zeta$ and $\partial^2\phi/\partial^2 y + \partial^2\phi/\partial^2 z = \sigma$. Here, the stream function and velocity potential are decoupled, the unknown parameters are functions of known values, and half as many equations with half as many unknowns need to be solved (however, they need to be solved twice: once for ψ and once for ϕ). For the aforementioned reasons, solving the Poisson equations is usually a better approach.

It is also of importance to note that there is, however, one characteristic of the Maskell formulation that makes its application very computationally intensive, despite its simplicity and reasonably small measurement scan requirements. This has to do with the application of the boundary conditions. Although the measurement area is limited to the viscous wake, the computational area must be expanded to include the entire test section so that the two boundary conditions required in solving for the stream function and the velocity potential may be applied, which are that the wind-tunnel walls are streamlines ($\psi = 0$) and that there is no flow across the tunnel wall (i.e., $\partial\phi/\partial n = 0$). This results in the simultaneous solution of a very large number of equations with many unknowns, especially if the scan resolution is sufficiently high. For the current experiments, the measurements were conducted with a 1.2%c resolution in a test section measuring 86.4×122 cm (or 34×48 in.), thus resulting in over 100,000 equations with over 100,000 unknowns. Employing a direct method to solve this linear

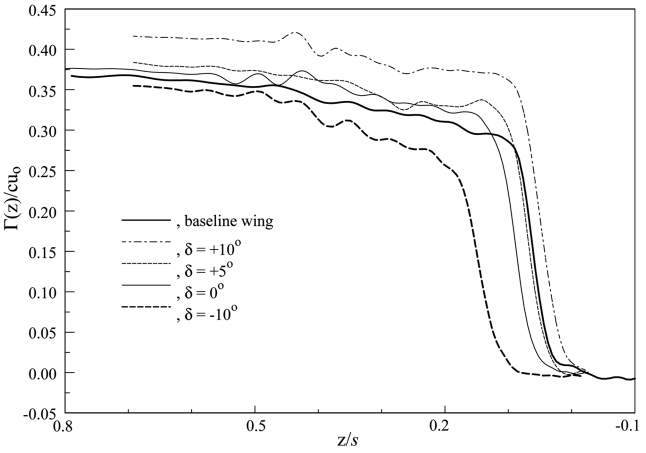

Fig. 9 Variation of normalized spanwise vorticity distribution with strake deflection angle for $\alpha = 10$ deg.

Table 1 Geometric dimensions and aerodynamic force coefficients at $x/c = 4$ and $\alpha = 10$ deg

δ, deg	S, cm^2	AR	S, cm	C_L	$\Gamma_{b,\mathrm{I}}/cu_o$[a]	$\Gamma_{b,\mathrm{II}}/cu_o$[b]	C_D	$C_{Di,\mathrm{I}}$[c]	$C_{Di,\mathrm{II}}$[d]
					Baseline wing				
N/A	1031.2	2.5	50.8	0.731	0.366	0.365	0.0513	0.0363	0.0260
					MTS wing				
−10	1115.5	3.14	59.2	0.729	0.365	0.358	0.0486	0.0279	0.0209
−5	1115.5	3.14	59.2	0.754	0.377	0.375	0.0513	0.0307	0.0215
0	1115.5	3.14	59.2	0.780	0.390	0.385	0.0485	0.0330	0.0248
5	1115.5	3.14	59.2	0.783	0.392	0.395	0.051	0.0351	0.0272
10	1115.5	3.14	59.2	0.811	0.406	0.420	0.0581	0.0363	0.0316

[a]$\Gamma_{b,\mathrm{I}}/cu_o = \frac{1}{2}C_L$. [b]$\Gamma_{b,\mathrm{II}}/cu_o$ is determined from Fig. 9. [c]$C_{Di,\mathrm{I}} = C_L^2/\pi e\mathrm{AR}_{\mathrm{eff}}$. [d]$C_{Di,\mathrm{II}}$ is computed via Eq. (2).

system of equations would be impractical without the use of a supercomputer.

One method that has been previously employed to circumvent this problem is to make use of Green's function to analytically solve the Poisson equation for

$$\psi(y,z) = -\frac{1}{4\pi}\iint \zeta(y_o,z_o)\log[(y-y_o)^2+(z-z_o)^2]\,\mathrm{d}y_o\,\mathrm{d}z_o$$

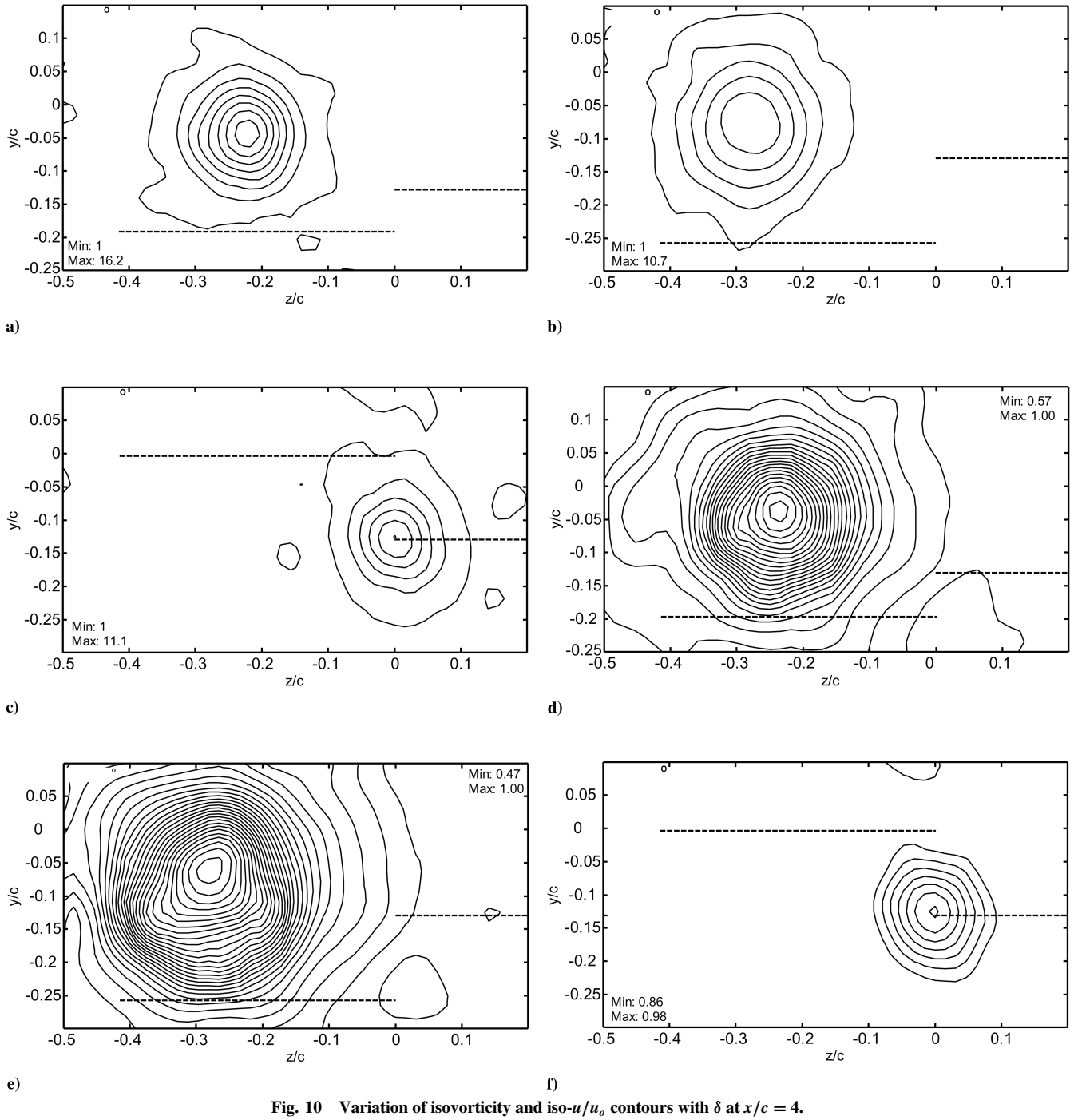

Fig. 10 Variation of isovorticity and iso-u/u_o contours with δ at $x/c = 4$.

and neglecting the contribution of ϕ [9,10,12]. It has been shown elsewhere that this method of calculating ψ is much more computationally efficient because it does not require an extension of the computational area; however, it does result in a slightly conservative estimate of the lift-induced drag: about 10% lower than the previous methods.

Another method that is roughly as computationally efficient as using Green's function, but nearly as accurate as directly solving the equations, and which is the technique employed in this study, is to use an iterative approach to estimate the solution of Poisson's equation. In addition, this method also allows the user to define the accuracy of the solution by discontinuing the iterative process when the desired tolerance has been achieved. A successive over-relaxation method [13], which is a modified form of the Gauss–Seidel technique, was applied and is described in the following systematic procedure. First, a centered finite difference computational scheme is applied to the Poisson equation, resulting in

$$\nabla^2\psi_{i,j} = (1/\eta^2)(\psi_{i,j+1} + \psi_{i,j-1} - 4\psi_{i,j} + \psi_{i+1,j} + \psi_{i-1,j} = \zeta_{i,j}$$

and

$$\nabla^2\phi_{i,j} = (1/\eta^2)(\phi_{i,j+1} + \phi_{i,j-1} - 4\phi_{i,j} + \phi_{i+1,j} + \phi_{i-1,j} = \sigma_{i,j}$$

where $i = 2$ to $n-1$ and $j = 2$ to $m-1$. This results in a linear system of $(n-2)\times(m-2)$ equations and $(n-2)\times(m-2)$ unknowns, which may be expressed in matrix form as $\mathbf{Ax} = \mathbf{B}$, where $\mathbf{A}$ is a matrix representing the Laplacian operator, $\mathbf{x}$ is a vector of unknowns (either ψ or ϕ), and $\mathbf{B}$ is a vector of known quantities (either ζ or σ). We then apply the information from the boundary conditions to the grid points adjacent to the boundary points. For example, on the lower test section wall, $\psi = 0$ and $\partial\phi/\partial n = 0$; therefore,

$$\nabla^2\phi_{2,j} = (1/\eta^2)(\phi_{2,j+1} + \phi_{2,j-1} - 3\phi_{2,j} + \phi_{3,j})$$

and

$$\nabla^2\psi_{2,j} = (1/\eta^2)(\psi_{2,j+1} + \psi_{2,j-1} - 3\psi_{2,j} + \psi_{3,j})$$

Note that although each equation has $(n-2)\times(m-2)$ unknowns, only five of them have nonzero coefficients; therefore, a matrix containing only the nonzero coefficients is necessary in the computation [i.e., the $\mathbf{A}$ matrix becomes an $(n-2)\times(m-2)$ by 5 matrix], provided that the indices of the unknown quantities on which each coefficient operates is retained. This significantly reduces memory requirements and increases the speed of the computation. Furthermore, because the $\mathbf{A}$ matrix is universal given the same computational grid, it may be saved and recalled for each computation. Note that due to the different boundary conditions, the $\mathbf{A}$ matrix varies slightly when applied to the velocity potential and when applied to the stream function.

Furthermore, being an iterative technique, the successive over-relaxation method requires an initial approximation to the solution. An approach that minimizes the number of iterations required when executing the calculation is to downsample the original data set to a much coarser resolution and to use matrix algebra to obtain an exact solution. In this investigation, a coarse resolution of 1 in. was used, resulting in a fairly small $\mathbf{A}$ matrix: 1632 by 1632 in size. The $\mathbf{A}$ matrix was then inverted and multiplied with the $\mathbf{B}$ matrix to solve for $\mathbf{x}$, which served as the initial approximation. Along with the initial estimate, another parameter was required that defined the degree of relaxation:

$$\omega = 4/\{[2 + (4 - (\cos(\pi/n) + \cos(\pi/m))^2]\}$$

With these in hand, the $(n-2)\times(m-2)$ equations may be solved for the values of $\mathbf{x}$ by solving the following equation for each equation successively:

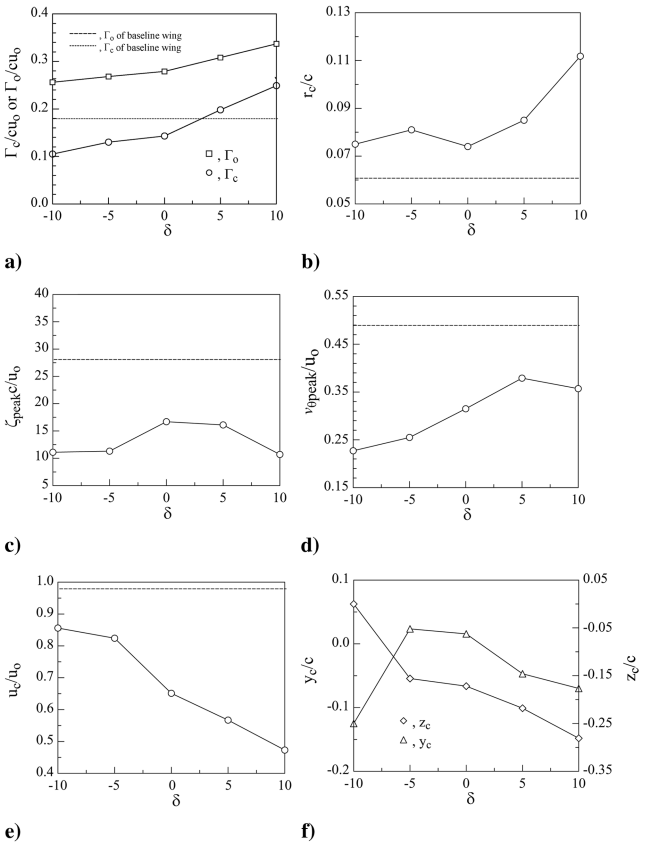

Fig. 11 Variation of critical vortex flow quantity with strake deflection angle at $x/c = 4$ for ; dashed lines indicate the baseline wing.

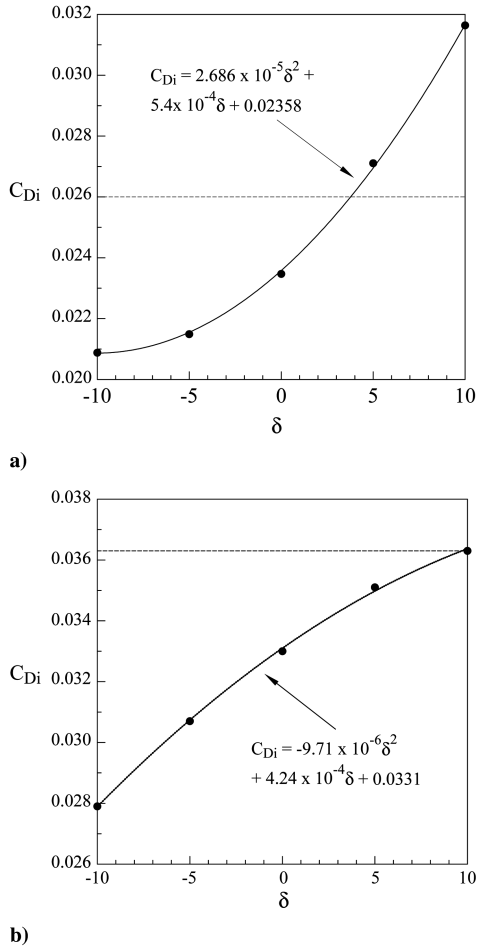

Fig. 12 Variation of C_{Di} with δ for $\alpha = 10$ deg: a) C_{Di} computed based on Eq. (2) and b) $C_{Di} = C_L^2/\pi e\mathcal{AR}$; dashed lines indicate the baseline wing.

$$x_i = (1-\omega)XO_i + \frac{\omega\left(-\sum_{j=1}^{i-1} a_{i,j}x_j - \sum_{j=i+1}^{n\times m} a_{i,j}XO_j + b_i\right)}{a_{i,i}}$$

where x_i is the variable being computed, XO_i is the initial approximation, $a_{i,j}$ is a value of the **A** matrix, and b_i is a value of the **B** vector. This computation is then repeated until the difference between the previous and newly iterated values lies within the predefined tolerance. The induced drag is then calculated as

$$D_i \approx \frac{\rho}{2}\sum_{j=2}^{m-1}\sum_{i=2}^{n-1}(\psi_{ji}\zeta_{ji} - \phi_{ji}\sigma_{ji})\eta^2 \tag{2}$$

The variation of the lift-induced drag coefficient C_{Di}, computed by using Eq. (2), with the strake deflection angle ($\delta = 0$, ± 5, and ± 10 deg) for $\alpha = 10$ deg is summarized in Fig. 12a. The value of C_{Di} was found to increase in a quadratic form with δ. The C_{Di} was, however, increased above that of the baseline wing for $\delta = +5$ and $+10$ deg strake settings, remaining below the baseline-wing value for $\delta = 0$, -5, and -10 deg strake settings. The C_{Di} was 23% higher and 20% lower than with the baseline wing for $\delta = 10$ and -10 deg, respectively. The larger the positive strake setting, the higher the C_{Di}, whereas the larger the negative δ, the smaller the C_{Di} value. The increase and decrease in C_{Di} agree well with the corresponding change in C_D, as well as with the aerodynamic gain and loss reported previously in Fig. 3b. It is also of interest to note that the C_{Di} computed via Eq. (2) is in disagreement with the values estimated directly by the following simple expression:

$$C_{Di} = \frac{C_L^2}{\pi e \mathrm{AR}} \tag{3}$$

where $e = e$ (AR and taper ratio) is estimated based on the suggestion of Anderson [14]. Figure 12b reveals that the magnitude of C_{Di}, estimated directly by using Eq. (3), increased nonlinearly with δ and was consistently below that of the baseline wing. Note that the C_{Di} value of the baseline wing estimated by using the $C_{Di} = C_L^2/\pi e \mathrm{AR}$ expression is higher (as much 40%) than that computed by using Eq. (1). Figure 12b further indicates that the C_{Di}, estimated via Eq. (3), was found to be 13 to 35% higher for the MTS wing, compared with the values computed via Eq. (2) at the same δ. Note that Eq. (3) is generally employed in high-Reynolds-number or intuitively inviscid flow conditions and can therefore serve as an upper bound of C_{Di} estimation for low-Reynolds-number flows, in which the viscous effects are dominant in addition to the potential breakdown of the strake LEV at a high strake setting.

IV. Conclusions

The effects of the strake setting, relative to the chord plane of the main wing on the wake vortex structure, and the lift-induced drag were investigated experimentally at $Re = 191,000$. It was shown that the presence of the strake led to an additional attached-flow lift and vortex lift and also energized the near-tip flow over the main wing as it progressed downstream and thus further increased its lift. In addition to its pronounced influence on the aerodynamic performance, the MTS wing-generated tip vortex also completed its roll-up process earlier than with the baseline wing and always led to a reduced peak tangential velocity and core axial velocity but an increased core radius. This core flow quantity was also generally found to increase with an increasing strake setting; however, the core and total circulation were observed to increase above the baseline-wing value for $\delta > 5$ deg and to decrease below the baseline wing for $\delta < 5$ deg. More important, the lift-induced drag, computed by using the Maskell induced-drag model, was found to increase nonlinearly with the strake setting and had a larger value than the baseline wing for a strake angle larger than about 5 deg. Further studies at higher Reynolds number and of the far-field vortex structures are needed. The net added aerodynamic gain resulting from the presence of the strake also needs to be quantified from the gain caused by the subsequent increase in the wing aspect ratio.

Acknowledgments

The work was supported by the Natural Sciences and Engineering Research Council (NSERC) of Canada. P. Gerontakos, L. S. Ko, and J. Pereira are thanked for their help with the experiment.

References

[1] Nikolic, V. R., "Moveable Tip Strakes and Wing Aerodynamics," *Journal of Aircraft*, Vol. 42, No. 6, 2005, pp. 1418–1426. doi:10.2514/1.4615

[2] Nikolic, V, R., "Planform Variations and Aerodynamic Efficiency of Moveable Tip Strakes," *Journal of Aircraft*, Vol. 44, No. 1, 2007, pp. 340–343. doi:10.2514/1.23490

[3] Nikolic, V. R., "Effect of Varying Leading Edge Form on Aerodynamic Performance of Wing-Moveable Tip Strake Configurations," *Journal of Aircraft*, Vol. 44, No. 5, 2007, pp. 1749–1753.

[4] Gerontakos, P., and Lee, T., "Near-Field Tip Vortex Behind a Swept Wing Model," *Experiments in Fluids*, Vol. 40, No. 1, 2006, pp. 141–155. doi:10.1007/s00348-005-0056-y

[5] Polhamus, E. C., "A Concept of the Vortex Lift of Sharp-Edged Delta Wings Based on a Leading-Edge Suction Analogy," NASA TN D-3767, Oct. 1966.

[6] Traub, L. W., "Implications of the Insensitivity of Vortex Lift to Sweep," *Journal of Aircraft*, Vol. 37, No. 3, 2000, pp. 531–533.

[7] Maskell, E., "Progress Towards A Method for the Measurement of the Components of the Drag of a Wing of Finite Span," Royal Aircraft Establishment TR 72232, 1973.

[8] Brune, G. W., "Quantitative Low-Speed Wake Surveys," *Journal of Aircraft*, Vol. 31, No. 2, 1994, pp. 249–255.

[9] Kusunose, K., "Development of a Universal Wake Survey Data Analysis Code," AIAA Paper 97-2294, 1997.

[10] Kusunose, K., "Drag Reduction Based on a Wake-Integral Method," AIAA Paper 98-2723, 1998.

[11] Betz, A., "A Method for the Direct Determination of Profile Drag," *Zeitschrift für Flugtechnik und Motorluftschiffahrt*, Vol. 16, 1925, pp. 42–44.

[12] Cummings, R. M., Giles, M. B., and Shrinivas, G. N., "Analysis of the Elements of Drag in Three-Dimensional Viscous and Inviscid Flows," AIAA Paper 96-2482, 1996.

[13] Burden, R. L., Faires, J. D., *Numerical Analysis*, 6th ed., Brooks/Cole, Florence, KY, 1997, Chap. 7.3.

[14] Anderson, J. D., *Fundamentals of Aerodynamics*, 2nd ed., McGraw–Hill, New York, 2005, pp. 338–340.